INTERNATIONAL JOURNAL OF MARITIME TECHNOLOGY

IJMT Vol.15/ Winter 2021 (79-91)

Experimental and numerical analysis of Hydrodynamic Characteristics of a surface piercing propeller mounted on high-speed craft

Mojtaba Pakian Bushehri[1], Mohammad Reza Golbahar Haghighi[2*]

[1] *PhD Student, Department of Mechanical Engineering, Persian Gulf University; pakianm@chmail.ir*
[2] *Associate Professor, Department of Mechanical Engineering, Persian Gulf University; golbahar@pgu.ac.ir*

ARTICLE INFO

Article History:
Received: 11 Apr. 2021
Accepted: 23 Aug. 2021

Keywords:
Surface Piercing Propeller
Propeller Torque and Thrust
Submerged State
Semi- Submerged State
Computational Fluid Dynamics

ABSTRACT

Surface piercing propellers are widely employed in high-speed crafts due to having many favorable features. These propellers operate at both submerged and semi-submerged states. In submerged state, to enhance the propeller hydrodynamic performance, the blades are usually manipulated through artificial ventilation by adding the air duct which is located at the propeller suction side. In current study, a 5-blade propeller proficiency has been studied under different operational conditions of 16 m catamaran vessel experimentally, the sea trial, and numerically using Computational Fluid Dynamics (CFD). The propeller behavior has been investigated under four sea trials while the propeller torque has been sampled at different engine states and vessel speed. The numerical study through CFD has been done to analyze the propeller behavior under different conditions, submerged and semi-submerged states. The numerical results have been validated by experimental observations. The propeller proficiency has been studied in two vessel motion stages which are pre-planing and post-planing. The results depict that the maximum torque is observed in submerged state at the last step of pre-planing mode while the engine speed is 2300 rpm. The propeller torque is reduced 10 to 16% at 2500 rpm in post-planning stage. In submerged state, the propeller proficiency is negligible at pre-planing mode.

1. Introduction

Surface piercing propellers are used on high-speed planing craft to achieve high speeds. The most common type of these propellers is supercavitating propellers, which reduces torque on the blades using ventilation. The propellers operate at different immersion depths by mounting on high-speed planing craft. Figure 1 shows the mentioned propeller position relative to the free surface of water in the pre- and post-planing stages of vessel motion.

Figure 1. Propeller position; (a): submerged (pre-planning stage) and(b): semi-submerged (post- planning stage).

These propellers have a sharp leading edge and a thick trailing edge. In addition, these kinds of propellers effectively reduce possibility of cavitation phenomena because of using ventilation.

According to the immersion depth, the ventilation mechanism in these propellers is different. Basically, there are two modes, sectional ventilation and full ventilation. In sectional ventilation, the cavitation effects or air bubbles on wake, near the trailing edge, can be seen while in full ventilation the whole of blades are covered with air bubbles from the leading edge to the trailing edge on the suction side. The occurrence of ventilation type depends on various factors such as the advance coefficient and the immersion depth. Artificial ventilation occurs in submerged state by using the air duct located at suction side of propeller while the vessel is in pre-planning stage.

Numerous studies have been carried out on surface propellers since 1953 including experimental, theoretical and numerical methods. Most of these studies performed on such propellers have been devoted to the study of the hydrodynamic characteristics, such as torque, thrust, efficiency and the ventilation mechanism. The effects of propeller geometrical characteristics (such as diameter, pitch as well as number of blades), and physical operating conditions of the propeller (such as the Reynolds, Weber, and Fraud numbers) on hydrodynamic characteristics or ventilation regime have been studied. Later, these studies became basis for the next studies. Particularly, the experiments which was performed by Olofsson [1] in his PhD thesis, was employed as the basis for the numerical simulation by some research. In the 21st century, with the development of computers and computational fluid dynamics methods, numerical

[Downloaded from ijmt.ir on 2026-09-10]

studies on these propellers have increased. CFD simulations with the Reynolds-Averaged Navier-Stokes (RANS) model have been widely used for surface piercing propellers. By implementing this model, turbulent flow and its effects around a propeller can be simulated. Caponnetto [2] simulated a surface piercing propeller using the RANS method and $k-\varepsilon$ model as turbulent model. His results were compared with Olofsson experimental data. Ghasemi [3] performed numerical analysis of two surface-piercing propeller models with three and six blades using BEM. Califano and Steen [4] discussed various mechanisms for propeller ventilation. They studied results of full ventilation in different conditions. Himei [5] simulated a surface-piercing propeller using RANS equations and VOF model. He simulated a ventilation mechanism and compared it with experimental results. Shi et al. [6] simulated velocity field around a five-bladed surface-piercing propellers. The numerical simulations were done at low immersion depth based on an experimental test. Alimirzazadeh et al. [7] investigated the immersion ratio effect and yaw angle on the performance of an 841-B surface-piercing propeller in inclined current. As they concluded, by increasing the immersion ratio, the results show that the torque and thrust coefficients increase and the efficiency decrease. Yari and Ghasemi [8] studied ventilation mechanism and the forces acting on the 841-B surface piercing propeller. They found that the cup on the blades has a significant effect on ventilation pattern, pressure distribution, and force. Javanmardi and Ghadimi [9] studied hydro-elastic and hydrodynamic analysis of a surface piercing propeller. They investigated the behavior of flow around the propeller as well as the pressure and stress applied to the blade surface at different angles and rotations. Yari and Ghasemi [10] studied the partial submerged propellers (PSPs) in order to reach a reliable performance prediction method with regard to the ventilation flow around PSPs. They used RANS equations and then compared numerical and experimental results. Based on this comparison, the terms of forces/moments and ventilation have very good agreement with the experimental data at a higher advance velocity ratio. Seyyedi and Shafaghat [11] presented the design algorithm of a free surface water tunnel to test the surface piercing propeller. They described construction stages of the free surface cavitation tunnel of Babol Noshirvani University of Technology. The calculation of its various sectors such as elbows, nozzle, settling chamber, test section and diffuser were given as well as calculation of pressure drops, proper pump selection and dynamometer. Shora et al. [12] simulated the hydrodynamic performance of a propeller under different geometrical and physical characteristics by using computational fluid dynamic (CFD). In CFD simulations, propeller thrust, torque and cavitation volume are computed with different pitch ratio, rake and skew angle, advance velocity ratio and cavitation number. Thrust and torque of the propeller is increased by enhancement of pitch ratio and positive values of rake angle. Yari [13] presented a numerical solution for predicting unsteady hydrodynamic forces acting on surface piercing propeller. He used RANS solver and sliding mesh method. He discussed ventilation pattern, pressure distribution and unsteady forces/moments on key blade. Javanmardi et al. [14] investigated flow around a cross section of surface hydrofoil through numerical modeling. They analyzed the effects of atmospheric pressure on hydrofoil hydrodynamics for two different cavitation numbers. Seyyedi et al. [15] studied hydrodynamic coefficients of propeller. They evaluated accuracy of some relations of determining hydrodynamic coefficient. The results showed no correspondence between semi-experimental relations and experimental data. Finally, they presented a suitable algorithm for selecting the surface-piercing propeller. Yang et al. [16] examined artificial ventilation for a surface piercing propeller by using a vent tube located at the suction side of the propeller. By investigating the effect of the vent pipe diameter on the hydrodynamic characteristics of the surface-piercing propeller at the submerged state, they showed that after ventilation the torque and thrust are decreased, while the efficiency is increased. Ganji Rad et al. [17] studied ventilation pattern and the performance of a 5-blade surface piercing propeller at 33, 40, 50 and 70% immersion ratios. The results showed that the maximum torque, thrust and efficiency occurs at 70%, 70% and 33% immersion ratios, respectively. Nouroozi and Zeraatgar [18] used a numerical study on an 841-B surface piercing propeller in open water conditions. They performed a reliable simulation by solving Unsteady Reynolds-averaged Navier–Stokes (URANS) equations and VOF model for water surface. Seyyedi et al. [19] tested a 5-blade surface piercing propeller in free surface tunnel experimentally. They studied the effects of immersion ratio and shaft inclination angle on the efficiency and hydrodynamic coefficients. Comparison of the obtained results with quasi-experimental equations showed that the equations presented in different geometric conditions were not very accurate. The results also showed that by increasing the immersion ratio, the torque and thrust coefficients increase and the efficiency decreases. Javanmard et al. [20] simulated the flow around an optimized surface-piercing propeller with a specific blade cross section at immersion ratio of 0.3. The results showed that the highest thrust and efficiency occur at a rotation angle of 180 degrees. The total thrust decreases with increasing of advance ratio. Yari and Moghadam [21] stydied a new geometry of Surface-piercing propeller (SPP-841B). They used RANS model to investigate force excitation, ventilation pattern and wake formation of the partially submerged propeller with inclination angle. They found out that

[Downloaded from ijmt.ir on 2026-09-10]

with an increase in shaft inclination angle, propeller thrust, and torque coefficients increased, whereas the propeller efficiency was decreased. Yari and Moghadam [22] studied on BEM method to predict the performance of a surface piercing propeller with and without cup in open water conditions. The ventilation pattern is in good agreement with the experimental results for a B-841 propeller. Torque and thrust coefficients are compared during a rotation with and without the cup. Seyyedi and Shafaghat [23] reviewed studies on surface piercing propeller. They divided these studies into three sections: experimental studies, experimental and theoretical studies, theoretical and numerical studies.

These types of propellers have been investigated many times in various literatures as a separate element from the vessel, but their behavior according to the movement of a vessel has not been studied. In this paper, the performance of a surface piercing propeller mounted on a 16-meter catamaran planning vessel in both submerged and semi-submerged states has been studied experimentally and numerically, and the results were compared in torque, thrust, and efficiency. This study provides a good understanding of the behavior of these propellers in accordance with the vessel motion and by studying torque and thrust in pre- and post-planing stages, the effect of its performance on the vessel is determined. In the numerical study, open water test carried out in submerged and semi-submerged states. In simulation at submerged state, the air duct is located behind and above the blades according to the shaft line of the vessel and by rotating the propeller, ventilation is done on the blades. This kind of research has been rarely performed and can be a clue to new studies. Pre planing mode is one of the most important stage of the vessel motion and the propeller is in the submerged state and the good performance of the propeller has a great impact on the ship planing.

2. Materials and Methods

2-1. Materials

In this study, the surface piercing propeller is a supercavitating propeller. It is shown in Figure 2 and its specifications are presented in table 1. This propeller is mounted on an ambulance catamaran vessel with planing hull and the vessel specifications are presented in table 2. Figures 3 and 4 show the vessel and the shaft line, respectively. As it can be seen from the shaft line, there is an air duct located at the suction side of the propeller. This duct creates artificial ventilation when the propeller is in submerged state. The air duct angle is zero relative to the vessel base line.

Table.1 Propeller specification

Characteristic	Value
Diameter	770 [*mm*]
Pitch	980 [*mm*]
No. of Blades	5
EAR	75 %

Table.2 Vessel Particulars

Characteristic	Value
Length	16 [*m*]
Width	4.4 [*m*]
Draft	0.9[*m*]
Tunnel B	1.5 [*m*]
Max Speed	44.5 [*Knots*]

2-2. Methods

In order to analyze the propeller, experimental and numerical methods have been used.

2-2-1. Experimental Methods

In the experimental method, the propeller is analyzed by an ambulance vessel. Propeller torque is obtained by installing a torque measuring device. The torque measuring device includes strain gauge, digital wireless torque telemetry and data acquisition system. The propeller torque in fully submerged and semi-submerged states was estimated for engine speeds of 1100 to 2800 rpm. The gearbox reduction ratio is 1.5 so; the propeller speed varies from 733 to 1866 rpm.

Figure 2.Surface piercing propeller used in this paper

Figure 3. View of the high speed planing craft

[Downloaded from ijmt.ir on 2026-09-10]

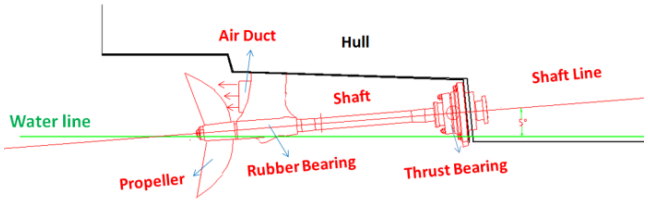

Figure 4. Shaft line of the propulsion system

2-2-1-1. Testing Process

The torque measuring device installed, and sea trials performed. Figure 5 shows the elements of torque measuring device. The strain gauge sensors are useful measurement tools to measure torque. Mechanical torque is input of the strain gauge and its output is a signal in millivolt.

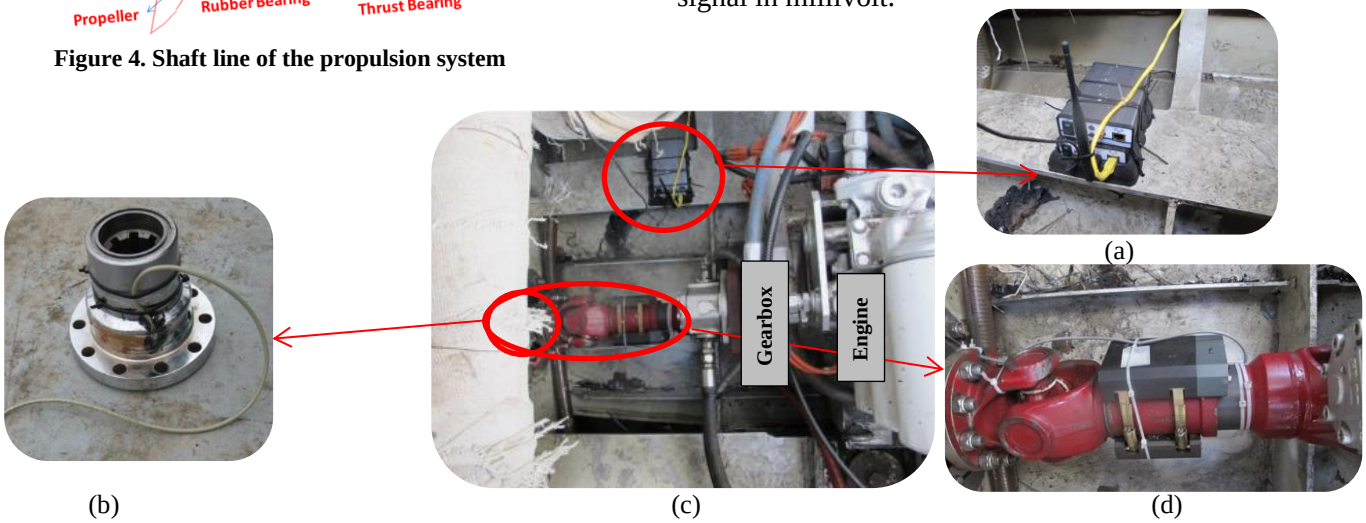

Figure 5. Installation of the torque measuring device; (a) Telemetry system (b) Strain gauge mounted on the coupling (c) Engine room (d) Cardan shaft and transmitter module

The input of telemetry system is a voltage and amplifies at the output. The transmitter module sends the signal to receiver module by wireless connection. The input of data acquisition system is voltage and torque value is output. Figure 6 shows schematic of torque measuring device.

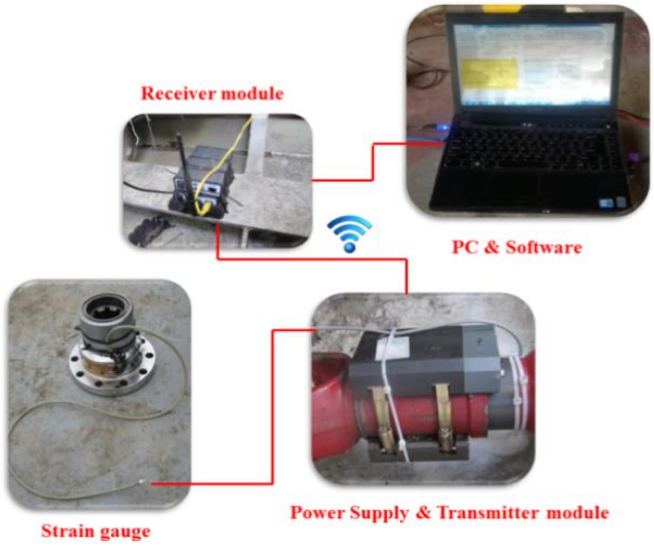

Figure 6. Schematic of torque measuring device

2-2-1-2. Calibration

At first, torque measuring device needs to be calibrated. The beam with length of 3 meters was selected and was connected to the coupling on one side, where the strain gauge sensor was installed, and loading was performed on the other hand. Figure 7 shows the calibration setup. The coupling was fixed by the workshop column (Figure 7- a). The beam length is based on the maximum torque. The calibration weights were selected to create various torques. The output data of the setup was read by torque measuring device and Additel calibrator. The model of calibrator is ADT 221A and shown in Figure 7-d. This device connects to the wires of the coupling sensor directly and shows the output voltage of the coupling in millivolts.

Loading was done by specific weights, which was measured by a digital scale with an accuracy of 50 grams. The loading was done, and in each stage, the weights were placed on the beam with a certain length. The calibration process was performed in two directions, clockwise and counterclockwise. Each test was repeated three times to check out the accuracy. Table 4 shows an example of the calibration results in two directions for the torque measuring device and Additel calibrator which has been repeated in three times.

As it can be seen clear from table 3, the results are close to each other and have an acceptable error with the calibrator.

Calibration coefficients for right and left setups are presented in tables 4 and 5. The calibration coefficients are close to each other and there is 4% and 3% error between minimum and maximum coefficient in the left and right setup, respectively. The calibration coefficient of the maximum applied load is selected for each setup.

[Downloaded from ijmt.ir on 2026-09-10]

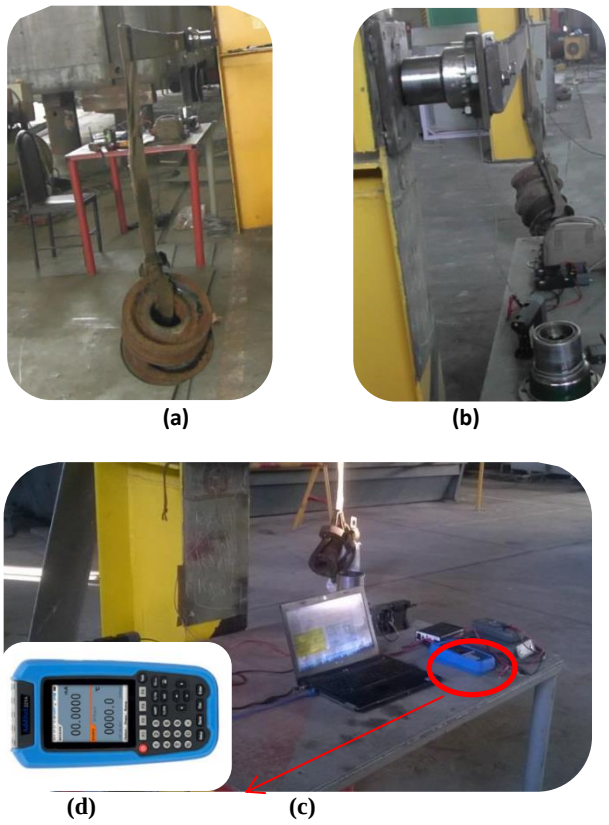

Figure 7. Calibration setup; (a): connecting coupling to the column (b): loading with weights (c): torque measuring device (d): Additel Calibrator.

Table 3. Example of calibration results in two directions

Test	Clockwise	Counterclockwise
First reading (N-m)	10902	11040
Error (calibrator criterion)	0.2%	0.8%
Second reading(N-m)	11058	11080
Error (calibrator criterion)	0.2%	1.3%
Third reading(N-m)	10975	11013
Error (calibrator criterion)	0.3%	0.6%

2-2-2. Numerical Methods

In the numerical method, by using capabilities of STARCCM+, the propeller was simulated in both case of submerged and semi-submerged. At first, after 3D scanning and cloud point production, propeller geometry was modeled in Rhino ceros [24, 25].

For a non-compressible Newtonian fluid, the RANS equations are defined according to Eq. (1).

$$\rho \frac{\partial(U_i)}{\partial t} + \rho U_j \frac{\partial U_i}{\partial x_j} = -\frac{\partial p}{\partial x_j} + \frac{\partial}{\partial x_j}\left(2\mu S_{ji} - \rho\overline{u_j' u_i'}\right) \quad (1)$$

Table 4. Calibration coefficient for the left setup

Torque (N-m)	0	600	1200	1800	2400
Shear strain	0	1.14E-05	2.29E-05	3.44E-05	4.59E-05
Voltage (mV)	0.65	0.68	0.71	0.74	0.77
Correction factor	-	19817.4	20689.6	20431.3	20083.6

Table 5. Calibration coefficient for the right setup

Torque (N-m)	0	600	1200	1800	2400
Shear strain	0	1.14E-05	2.29E-05	3.44E-05	4.59E-05
Voltage (mV)	1.28	1.33	1.38	1.43	1.48
Correction factor	-	12396.6	12195.1	12000	12207.5

In Eq. (1), U_i is velocity vector and t, P and μ are time, pressure and dynamic viscosity, respectively. S_{ij} is the mean strain rate and u' is varying component of velocity. RANS equations in three-dimensional space also with the mass continuity equation result in four independent equations with ten unknown variables. The inequality between number of equations and unknowns makes it impossible to solve this problem analytically. On the other hand, presence of Reynolds stresses ($\rho\overline{u_j' u_i'}$) increases the complexity of this problem. To solve such a problem, usually Reynolds stresses are modeled using viscosity models on linear vortices. For this purpose, Eq. (2) must be established.

$$-\rho\overline{u_j' u_i'} = 2\mu_t S_{ji} - \frac{2}{3}\rho k \delta_{ij} \quad (2)$$

In Eq. (2), μ_t is called turbulent viscosity or vortex viscosity, k is turbulent kinetic energy and δ_{ij} is the Kronecker delta. Turbulent viscosity can be estimated using several methods. One of these methods is to use a two-equation model (for example, the k-ε turbulence model). Volume of fraction (VOF) is used for modeling water free surface, and ISO surface is used to display the water level. When volume of a water cell is reduced by half, it indicates as the free surface or two-phase fluid.

According to STARCCM+ user guide [26], implicit unsteady model is used for two-phase flows and Eulerian multiphase is selected for modeling two-phase flow. So as to model turbulence, K − ε is selected.

3. Result

3-1. Sea Trials

Four sea trials conducted, and propeller torque is recorded and shown in terms of engine speed (rpm). Sea trial has been conducted in Bushehr port and sea state checked in each sea trials. Figure 8 shows torque and engine rpm over a period of 17 minutes at 1800 rpm. The torque at 1800 rpm oscillates over 3090 N-m. Torque and thrust values of surface piercing propeller are oscillating. The final torque is average torque for a specified engine rpm.

The first test was conducted in calm sea, in sea state 1. The wind speed was measured 3 km/h. The graph of torque and engine rpm is shown in Figure 9. As it can be seen in the diagram, torque increases from 1100 to 2300 rpm. At 2300 rpm, while the vessel starts the

[Downloaded from ijmt.ir on 2026-09-10]

planning mode, propeller changes position from submerged to semi-submerged and torque decreases. After complete planning stage at 2500 rpm, it grows again. The torque at the pre-planning stage is about 10% higher than the post- planning stage. The right torque is about 10% higher than the left one at 2800 rpm.

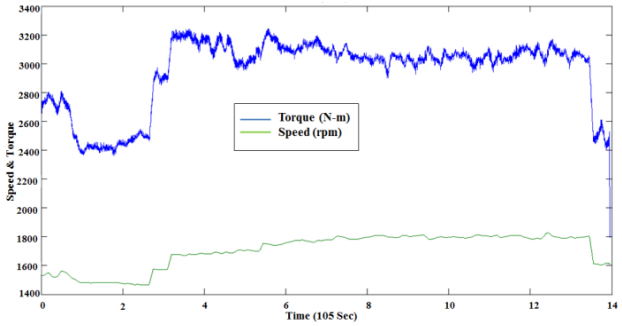

Figure 8. Torque/ engine rpm and time over sea trial

The second test was conducted in sea state 1 and the vessel was head sea. The wind speed was measured 5 km/h. The torque diagram is shown in Figure 10. The right torque in the pre-planning stage at 2300 rpm is 9% more than the post- planning stage at 2500 rpm and this difference in the left torque is 16%. The right torque is about 15% higher than the left torque at 2800 rpm.

The third test was performed in sea state 1 and the vessel was flowing sea. The wind speed was measured 6 km/h. The torque diagram is shown in Figure 11. As it can be seen from the diagram, the right torque in the pre-planning stage at 2300 rpm is 16% more than the post- planning stage at 2500 rpm and this difference in the left torque is 12%. The right torque is about 12% higher than the left torque at 2800 rpm.

Values of vessel speed and propeller speed are presented in table 6, which are the result of sea trials in full-load condition.

Table 6. Vessel speed and propeller rpm at full displacement

	Propeller state	Speed Knots	Engine rpm	Propeller rpm
1	Submerge	7.8	1100	733
2	Submerge	11.6	1600	1067
3	Submerge	16.2	2100	1400
4	Semi-Submerge	25.3	2500	1666
5	Semi-Submerge	36.9	2700	1800
6	Semi-Submerge	44.5	2800	1867

3-1-1. 10% of Displacement Reduction

The fourth test was conducted in calm sea and the vessel was head sea. The wind speed was measured 5 km/h. In this test, 2 tons of total weight of vessel reduced by reducing of fuel and water volume. Torque values are shown in Figure 12 with respect to engine rpm. Here, the right engine generates more torque than the left one, too. The torque in the pre-planning stage at 2300 rpm is about 12% higher than the post-planning stage. Data from the previous test, where the weight was about 10% higher, are shown in solid squares and rhombuses. Torque comparison between third and fourth tests is shown in Figure 13. Torque of the previous test is shown with triangle and multiplication symbol. The torque reduced about 10% to 16% compared to the previous test at the pre- and post- planning stage and the maximum vessel speed. The difference between the torque right and left in the previous test was about 12%, but in the new test is 16% at the maximum speed.

Figure 14 shows comparison between propeller torque at 2300, 2500 and 2800 engine rpm which are related to pre- planning, post- planning stages and the final speed of the vessel, respectively. In the second, third and fourth trials, the right torque in the final engine speed is higher than the pre-planning stage, while the left torque in the final engine speed is less in all the sea trials. This indicates that the operating conditions of the right propeller are more difficult.

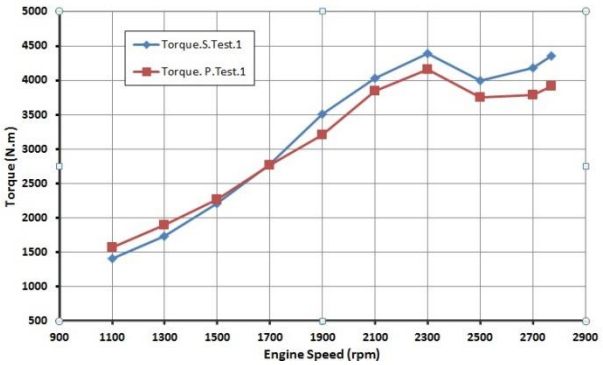

Figure 9. Propeller torque values in the first sea trial

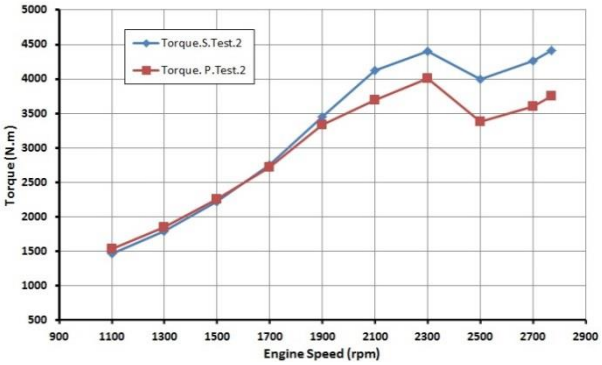

Figure 10. Propeller torque values in the second sea trial

[Downloaded from ijmt.ir on 2026-09-10]

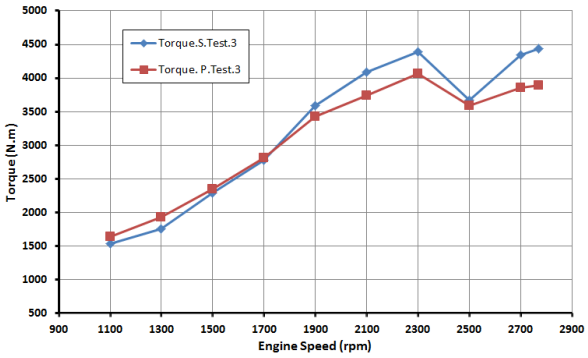

Figure 11. Propeller torque values in the third sea trial

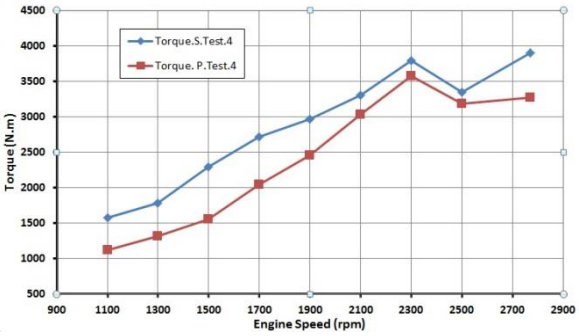

Figure 12. Propeller torque values in the fourth sea trial

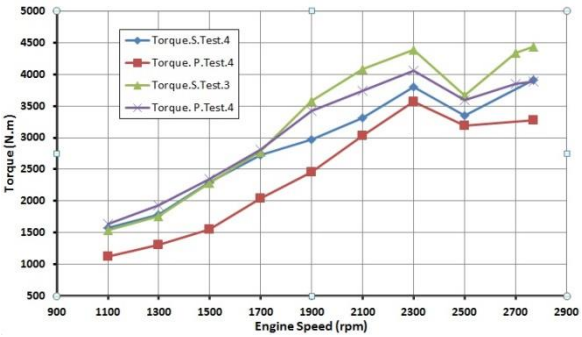

Figure 13. Comparison of propeller torque in the third and fourth sea trials

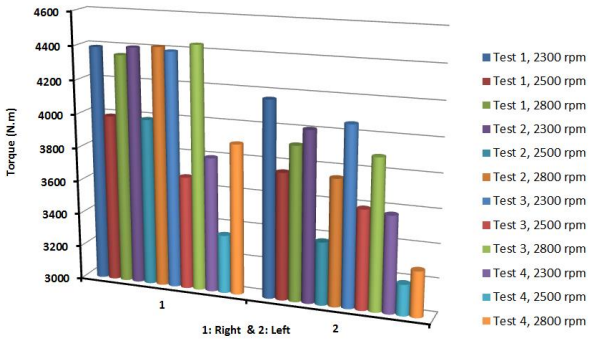

Figure 14. Comparison of right and left torque at 2300, 2500 and 2800 rpm

3-1-2. Uncertainty Analysis

At these experiments, there are some error sources like any other measurements. The calibrations and the accuracy of sensors are main error sources for the presented results. Vessel speed measured by the GPS with 0.1 knot accuracy equals to 0.2% error. The engine speed accuracy is also about 50 rpm that implies 1.7% error in the measurements. Also, the propeller torque is measured with an accuracy of the 1.3 Percent. Based on the uncertainty analysis calculations, the overall uncertainty for the presented results are about 2.1 percent.

3-2. Numerical Solution

Reynolds-averaged Navier–Stokes (RANS) equations must be solved by using Reynolds Stress. The propeller has been simulated in two cases: a) submerged b) Semi-Submerged.

After modeling the propeller geometry, the propeller and part of shaft have been analyzed. The process of analyzing propeller hydrodynamic performance has been done in StarCCM+. Figure 15 demonstrates the propeller and shaft with 5 degrees of shaft line angle. As Figure 15 shows, in order to take effects of shaft on the propeller, and simultaneously decreasing the computational time, just 10 and 70 cm of propeller shaft was modeled for submerged and semi- submerged state, respectively. In semi- submerged state, due to the free surface effects, the longer shaft is selected.

For simplification in numerical simulation, propeller simulations have been done under conditions of open water test in two cases of submerged and semi-submerged according to sea trials (Propeller rpm and ship speed). To compare the sea trials and the propeller open water test, it is necessary to calculate the water inlet speed to computational field. The wake coefficients are required to calculate the advance speed. The value of the wake coefficient can be determined by regulation formulas for different hulls and with characteristic conditions. It is known that the velocity distribution behind the transom is not the same so, calculating the wake factor and assuming the same velocity distribution led to the little error relative to the sea trial. However, due to the existence of experimental test results and the purpose of this study, which is to investigate the behavior of propeller (The process of changes in torque, thrust and efficiency in different operating conditions of a planing vessel and not their exact amount) the amount of error is acceptable.

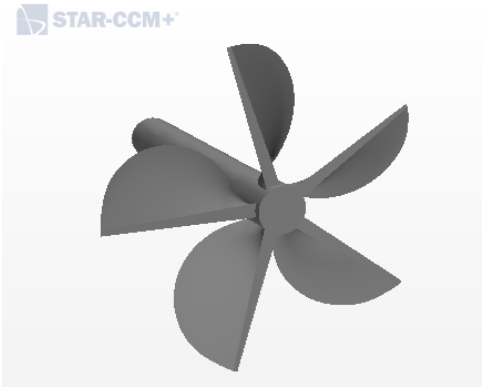

Figure 15. Propeller geometry and its 70 cm shaft in StarCCM+.

The approximate values of the wake coefficient are calculated using the Taylor formula for a twin-screw vessel [27]. The Eq. (3) and Eq. (4) are presented the Taylor formula and advance speed, respectively.

$$W = 0.55C_B - 0.2 \quad (3)$$

$$V_a = V_s(1 - W) \quad (4)$$

[Downloaded from ijmt.ir on 2026-09-10]

Where, C_B , V_a , V_s and W_f are the block coefficient, advance speed, ship speed and wake coefficient. The values of the block coefficients are obtained in towing tank for model of the vessel. This test was performed in the twin tank of Stellenbosch University in South Africa and model is scaled to 1:11.43. In all testes, total resistance and trim have been investigated in various LCG. The wake coefficient values are presented in table 7 for engine speed of 1100, 2100, 2500 and 2800 rpm.

Table 7. Approximate values of the wake coefficient

	Engine Speed (rpm)	Ship Speed (knots)	C_B	Wake coefficient
1	1100	7.8	0.531	0.09
2	2100	16.2	0.275	- 0.04
3	2500	25.3	0.418	0.03
4	2800	44.5	0.402	0.02

The value of wake is negative at 2100 rpm. At this point, the vessel is in hump region and the trim angle is 8 degrees. The negative value indicates the Taylor formula is not suitable for this point. Therefore, the ship speed is selected as advance speed of propeller at this point.

Figures 16 and 17 demonstrate boundary conditions for two cases of simulation. According to previous study, the computational domain was chosen in such a way that it did not affect the results. Here, the domain is a cylinder. It has diameter of 6D and length of 13D, which D is propeller diameter [9, 12, 13, 16, 17, 18, 20, 21].

In state of fully submerged, air blows at suction side of blades through a duct. Air above of the water free surface is directed through it. The degree of ventilation is zero relative to water free surface and the trim angle of the vessel is not considered in all simulation. As a result, a two-phase flow (Water and Air) flows around the blades. The propeller modeled with same shaft angle, and air duct is located 5 cm behind the propeller. Rigid body motion is used to simulate rotational movement of propeller. In the submerged state, the computational domain consists of the main cylindrical block that the cylinder around the propeller and the air duct are subtracted. The boundary between the main cylinder and the propeller cylinder is the interface.

In the semi- submerged state, the computational domain consists of the main cylindrical block that the cylinder around the propeller is subtracted. The boundary between the main cylinder and the propeller cylinder is the interface.

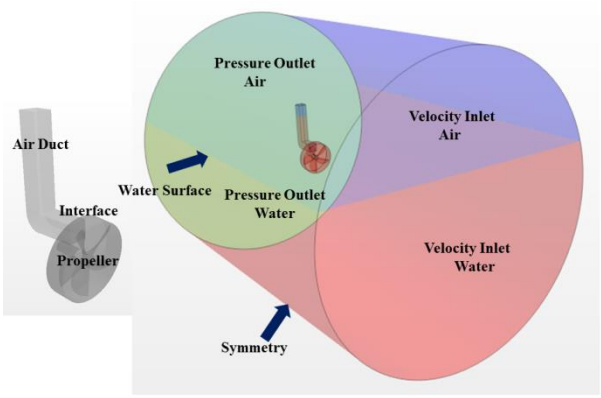

Figure 16. submerged state boundary conditions with air duct

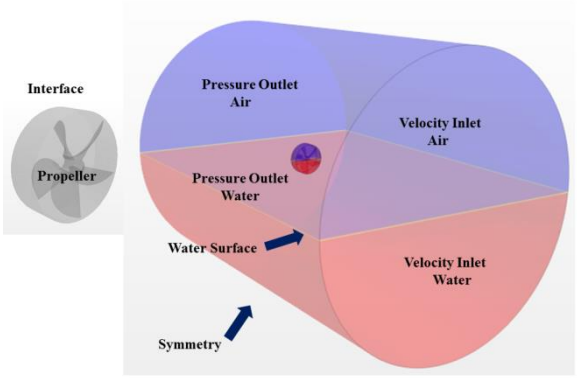

Figure 17. Semi- submerged state boundary conditions

For spatial discretization, three types of mesh need to be generated.

A) Volume Mesh: used for generating mesh in domain.

B) Surface Mesh: used for generating mesh on surfaces.

C) Boundary Layer Mesh: used for generating mesh in boundary layer next to the surfaces.

In this paper, spatial discretization (including three types of mesh) has been done by utilizing trimmer mesh, surface mesh and prism layer mesh for type A), B) and C), respectively. Because of importance of boundary layer, and necessity getting closer to reality, non-dimensional parameter y^+ is defined. y^+ indicates the distance of fist mesh next to geometry surface. This parameter can be estimated by Eq. (5):

$$y^+ = \frac{u_* y}{\nu} \quad , \quad u_* = \sqrt{\frac{\tau_w}{\rho}} \qquad \tau_w = C_f \times \frac{1}{2}\rho V^2 \tag{5}$$

Here, u_* is frictional velocity, y distance of first mesh from surface, τ_w wall shear stress, C_f frictional coefficient, ρ density and V velocity.

STARCCM+ user guide provides suggested y^+ values for each turbulent model and wall function. For instance, by using Realizable $\text{Two} - \text{Layer}\ k - \varepsilon$, which used in this paper, only all $- y^+$ is defined as a wall function. So, suggested y^+ values are $y^+ < 1$ or $y^+ > 30$.

[Downloaded from ijmt.ir on 2026-09-10]

The generated mesh for submerged and semi-submerged states are shown in Figures 18 and 19, respectively. It should be mentioned that in order to generate prism layer mesh, boundary layer thickness must be computed for each case with different velocity.

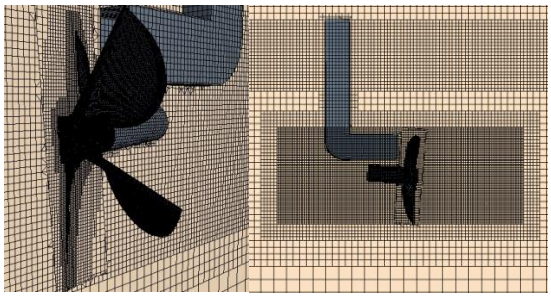

Figure 18. Generated mesh in computational domain for submerged state

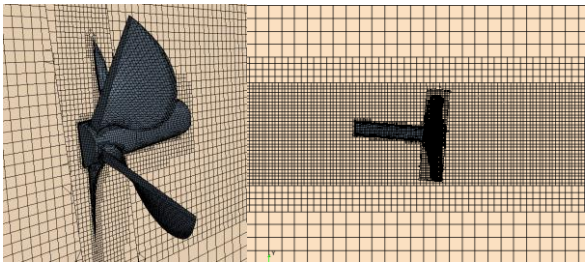

Figure 19. Generated mesh in computational domain for semi-submerged state

Results must be independent of mesh number. For this, mesh study has been done for submerged state and shown in Figure 20. What has been monitored throughout simulations is torque magnitude.

Numbers of mesh that have been studied in this case are 335000, 566000, 995000, 1400000, 2950000 and 5940000. There is 8.4% error by comparing the simulation result and the second sea trial result in mesh number of 5940000. The torque values in simulation with 1400000, 2950000 and 5940000 meshes are close together and as mesh number changes from 2950000 to 5940000, the difference in average torque is less than 1.3%. Here, 2950000 meshes have been chosen.

For semi-submerged case, average torque has been monitored with 1666 rpm. Numbers of mesh that have been studied in this case are 299000, 607000, 1050000, 1950000, 3030000 and 5965000. There is 7.1% error by comparing the simulation result and the second sea trial result in mesh number of 5965000. The Figure 20 shows the torque values are close in meshes 1950000, 3030000 and 5965000 and as mesh number changes from 3030000 to 5965000, the difference in average torque is less than 1.9%. Here, 3030000 meshes have been chosen.

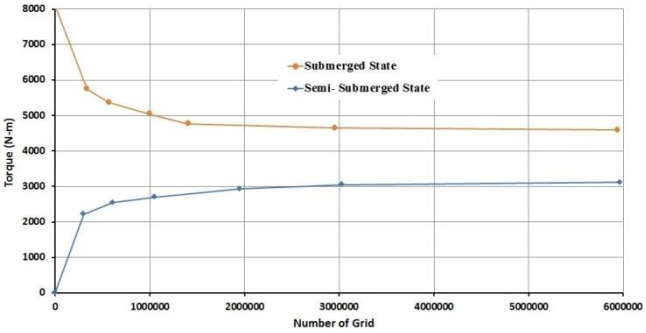

Figure 20. Mesh study for submerged and Semi- Submerged state

Figure 21 shows y^+ values for submerged and semi-submerged states. Here, propeller speed is 733 and 2500 rpm in submerged and semi- submerged state, respectively. As Figure 30 shows, y^+ range varies from 30 to 80 on most part of the propeller. Therefore, meshes next to the geometry are fine enough and boundary layer is modeled well. In this paper, turbulent viscosity can be modeled by using Realizable Two $-$ Layer $k-\varepsilon$. This model is combination of Realizable $k-\varepsilon$ with two-layer method. $k-\varepsilon$ is a turbulent model in which k is the turbulent kinetic energy and ε is turbulent dissipation rate. At first, in order to simulate propeller moment both $k-\varepsilon$ and $k-\omega$SST were used then, according to the results of each, $k-\varepsilon$ was chosen because of better results for convergence. Table 8 shows the solver setting of simulation. Time step and physical time are presented in t^*. t^* is shown in Eq. (6) that V and L are velocity of flow and propeller length, respectively.

$$t^* = \Delta t * {}^{V}/_{L} \qquad (6)$$

Table 8. Solver Setting of Simulation

	Simulation (rpm)	t^* Time Step	t^* Physical Time
1	1100	0.0037	7.4
2	2100	0.008	16.44
3	2500	0.0018	4.03
4	2800	0.003	6.3

To get numerical simulation done we implemented a computational system equipped by Intel® Core™ i9-9900k CPU @ 3.6HHz.

3-2-1. Results of Submerged state

In this case, simulations are done with engine speed of 1100 and 2100 rpm (propeller speed of 733 and 1400 rpm), and then, compare with result of sea trials. To simulate this state, time step of 0.0001 is chose. Results are included torque, thrust and residuals. Torque magnitudes are oscillating, it decreases as a blade reaches two-phase flow (because of air suction by duct) and it goes up when that blade passes two phase flows. So, torque has maximum and minimum values in each simulation and average torque was considered.

[Downloaded from ijmt.ir on 2026-09-10]

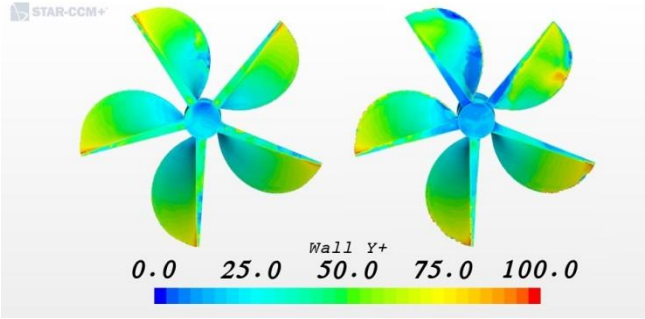

Figure 21. y^+ values for (Left): submerged state (Right): semi- submerged state

As the propeller starts to rotate, air is sucked by the duct. After the second blade passes the duct, other blades meet two-phase flow. Figure 22 shows ventilation pattern for the advance coefficient of 0.46 at submerged state. Red and green regions indicate water and mixture of water and air, respectively.

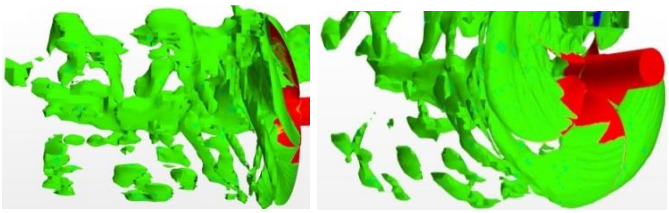

Figure 22. Ventilation pattern of submerged state

Torque magnitudes are given in Figure 23. The torque average is 1528 N-m and 4648 N-m at 733 and 1400 rpm, respectively. The average is calculated in one cycle of propeller rotation at 733 and 1400 rpm. This process is repeated at each propeller rotation after the results became steady. In both diagrams, 5 peaks can be seen that are correspond to the rotation of the 5 blades. Figure 24 shows errors in the numerical results with the first, second and third sea trials. At 1100 rpm, the results are closer to the sea trial. The error value increased at 2100 rpm in compassion to the sea trials. In fact, when propeller rpm and vessel speed are increased, dynamic trim in pre- planning stage is increased too. Because of different in dynamic trim and wake coefficient are not considered in the simulation (the wake coefficient was negative with the Taylor formula) in simulation, there is more error in the results of 2100 rpm. Oscillating domain of torque increased in the simulation at engine speed of 2100 rpm. It can be concluded that, as the propeller rpm and vessel speed rise, the oscillating domain of torque increases.

Figure 25 shows propeller thrust at 733 and 1400 rpm. The thrust average is 8.9 KN and 28 KN at 733 and 1400 rpm, respectively.

Advance coefficient, thrust coefficient, torque coefficient and Propeller efficiency are calculated by formulas 7 to 10.

$$J = \frac{V_a}{n_{prop} * D} \quad (7)$$

$$K_t = {}^{T}/_{\rho * {n_{prop}}^2 * D^4} \quad (8)$$

$$K_q = {}^{q}/_{\rho * {n_{prop}}^2 * D^5} \quad (9)$$

$$\eta = \frac{J}{2\pi}\frac{K_t}{K_q} \quad (10)$$

For advance coefficients of 0.38 and 0.46, the efficiencies are 27% and 30% for 733 and 1400 rpm, respectively.

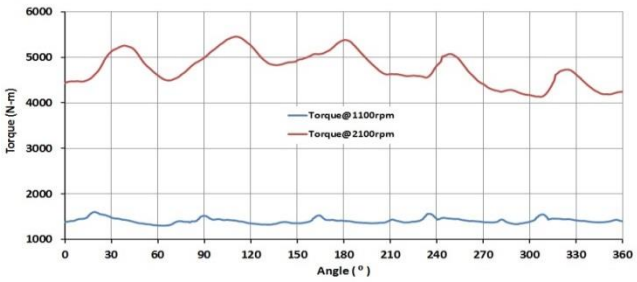

Figure 23. Propeller torque at engine speeds of 1100 and 2100 rpm

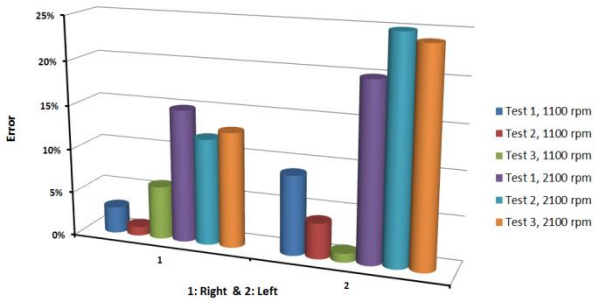

Figure 24. Error in the numerical results with the first, second and third sea trials in submerged state

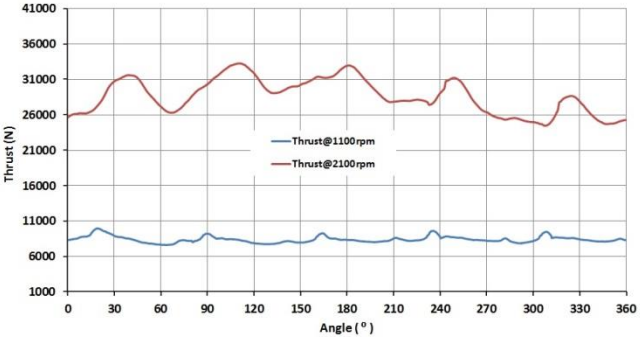

Figure 25. Propeller thrust at engine speeds of 1100 rpm and 2100 rpm

3-2-2. Results of Semi- Submerged state

In this case, the propeller was simulated at engine speed of 2500 and 2800 rpm. For these simulations, $\Delta t = 0.0001$ s. Figure 26 shows the wave on free surface. In this case, generally, two blades contact with water completely. In addition, the wave was generated over free surface and below free surface.

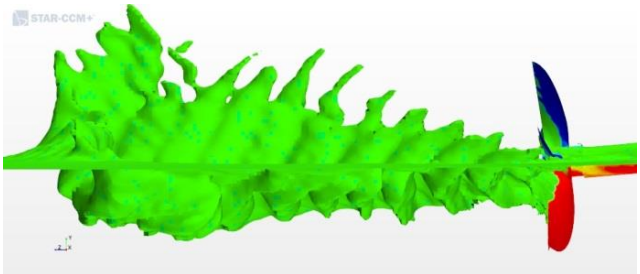

Figure 26. Ventilation pattern in semi- submerged

[Downloaded from ijmt.ir on 2026-09-10]

Propeller torque at engine speed of 2500 and 2800 rpm are shown in Figure 27. The torque average is 3050 N-m and ٣٦٢٠ N-m for engine speed of 2500 rpm and 2800 rpm, respectively. This process is repeated at each propeller rotation after the results became steady. There are 5 peaks that are corresponded to the rotation of the 5 blades in the diagram. Figure 28 shows errors in the numerical results with the first, second and third sea trials. In the left torque at 2800 rpm, the results are closer to the sea trial and errors are less than 10%. In some places, it is more than 20%. Some sea trial parameters are not considered in the open water test such as sea state, ship movement and so on. So, the torque can be different than the sea trials. Torque magnitudes are oscillating at engine speed of 2800 rpm. This can be concluded that as propeller rpm and vessel speed rise, the domain of torque oscillation increases.

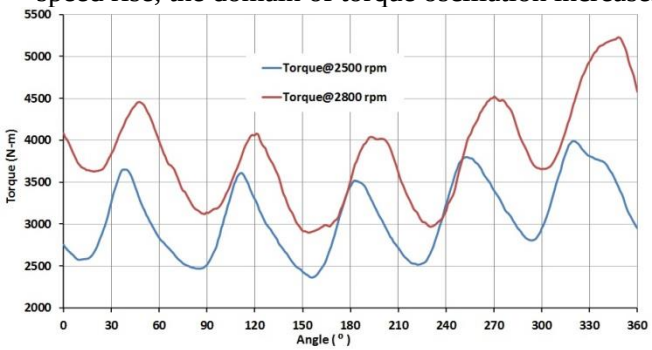

Figure 27. Propeller torque at engine speed of 2500 rpm and 2800 rpm

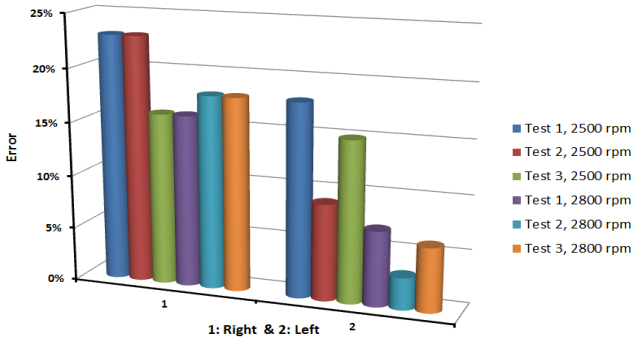

Figure 28. Errors of the numerical results with the first, second and third sea trials in semi- submerged state

Figure 29 shows propeller thrust. Thrust average for engine speed of 2500 and 2800 rpm are 19.82 KN and 21.35 KN, respectively. According to Eq. 5 to 8, for advances coefficient of 0.54 and 0.84, the efficiencies are 43% and 60% at 2500 and 2800 rpm, respectively.

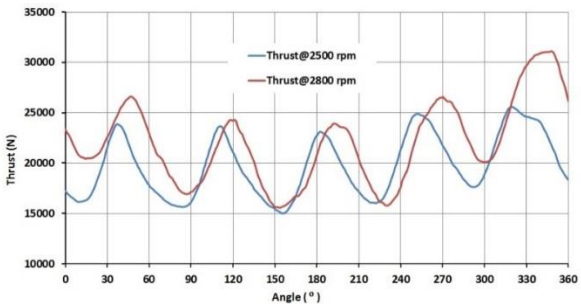

Figure 29. Propeller thrust at engine speed of 2500 rpm and 2800 rpm

4. Conclusion

In this paper, supercavitating surface piercing propeller proficiency under different operational conditions of 16 m catamaran vessel was analyzed. The propeller torques was measured at different engine speeds (rpm) and different vessel speeds. The torque measurement device was located on the propeller shaft. To experimental study four sea trials were performed. Under all conditions, the torque diagrams trend is getting increased, decreased and finally increased at pre-planning, post-planning, as well as top speed. The sea trials results confirm that submerged state at the last step of pre-planing state while the engine speed is 2300 rpm. At 2500 rpm, post-planning position, the propeller position is semi-submerged state. Under mentioned condition the propeller torque is reduced 10 to 16%. In fourth sea trial when the vessel deadweight was decreased the propeller torque at pre-planing stage was reduced significantly. Differences the right and left propeller torque can be find out through performing under different conditions. The right propeller torque is higher than the left one due to operating under heavy state of right one. Numerical simulation of propeller has been performed for submerged state at engine speed of 1100 and 2100 rpm and for semi-submerged state at 2500 and 2800 rpm. The propellers torque was also obtained numerically in open water test. Sea trial and numerical simulation measured torques depicts acceptable error so that they are close to each other in the submerged state at 1100 rpm. It should be considered that error criteria will be increased at engine speed 2100 rpm. However, results heterogeneous are more less for the left propeller torque at engine speed 2800 rpm in the semi-submerged state. The sea trial results also showed that the right propeller operating conditions are heavier. Effects of propeller rotation speed and water velocity on some important parameters such as torque, thrust as well as efficiency have been studied according to sea trial results in all numerical simulations. In submerged state, air is sucked by a duct which is located at the propeller suction side and artificial ventilation is performed on the propeller. In semi-submerged state, wake is generated underwater and above the water free surface at propeller pressure side. Fluctuation amplitude increases by increasing the propeller speed in rpm. When engine works at last step of pre-planning stage, the propeller torque and thrust are higher than the first step of post-planing stage while the vessel speed and propeller efficiency at last step of pre-planning stage are much lower than post-planing stage. The propeller efficiency is very low in the submerged state and the efficiency increases when the propeller is in the semi-submerged state. Low efficiency in submerged state is one of the weakest points in this propeller hydrodynamic characteristics. Artificial ventilation is one of the most important issues of high-speed planning crafts and has not been

[Downloaded from ijmt.ir on 2026-09-10]

extensively studied. Therefore, it is recommended to study the cross section of air duct, distance from duct to propeller, location and the angle of air injection in future research.

5. Symptom List

D	Propeller Diameter (m)
EAR	Expanded Area Ratio
J	Advance Coefficient
K	Turbulent Kinetic Energy
K_q	Torque Coefficient
K_t	Thrust Coefficient
L	Length (m)
n_{eng}	Engine speed (rpm, rps)
n_{prop}	Propeller speed(rpm, rps)
P	Pressure (Pa)
q	Torque (N-m)
T	Thrust (N)
t	Time (s)
V_a	Advance Speed (knots,ms^{-1})
V_s	Ship Speed (knots,ms^{-1})
p	Density (kg/m^3)
μ	Dynamic Viscosity ($N.s/m^2$)
η	Propeller Efficiency
μ_t	Turbulent Viscosity
U_i	Velocity Vector
S_{ij}	Mean Strain Rate
Δt	Time Step (s)
Δθ	Rotational Movement of Propeller (°)
t^*	Dimensionless of Time

6. Reference

[1]. Olofsson, N., (1996*), Force and flow characteristics of a partially submerged propeller*, Chalmers University of Technology, Doctoral thesis.

[2]. Caponnetto, M., (2003), *RANSE simulations of surface piercing propellers, 6th numerical towing tank symposium*, Numerical Towing Tank Symposium.

[3]. Ghassemi, H., (2009), *Hydrodynamic characteristics of the surface-piercing propellers for the planing craft*, Journal of Marine. Sci. Appl,V. 8, p. 267-274.

[4]. Califano, A., Steen, S., (2011), *Identification of ventilation regimes of a marine propeller by means of dynamic-loads analysis*, Journal of Ocean Engineering, V.31(14-15), P.1600-1610.

[5]. Himei, K., (2013), *Numerical analysis of unsteady open water characteristics of surface piercing propeller*. 3rd international symposium on marine propulsors, Launceston, Australia.

[6]. Shi, X.Y., Zhang, L.X., Shao, X.M., (2014), *Numerical study of the hydrodynamic performances of surface piercing propeller*, Journal of Mech & Electric Eng, V.31(8), p. 985–990.

[7]. Alimirzazadeh, S., Roshan, S.Z., Seif, M.S., (2016), *Unsteady RANS simulation of a surface piercing propeller in oblique flow*. Appl Ocean Research V.56, p. 79–91.

[8]. Yari, E., Ghassemi, H., (2016), *Numerical analysis of surface piercing propeller in unsteady condition and cupped effect on ventilation pattern of blade cross-section*. Journal of Mar Sci Tech, V. 21, p. 501–516.

[9]. Javanmardi, N., Ghadimi, P., (2016), *Hydroelastic analysis of semi-submerged propeller using simultaneous solution of Reynolds-averaged Navier–Stokes equations and linear elasticity equations*. Journal of Engineering for the Maritime Environment. V. 232, p. 199–211.

[10]. Yari, E., Ghassemi, H., (2016), *The unsteady hydrodynamic characteristics of a partial submerged propeller via a RANS solver*. Journal of Marine Engineering & Technology, v. 14 (3), p. 111- 123.

[11]. Seyyedi, S. M., Shafaghat, R., (2016), *Design Algorithm of a Free Surface Water Tunnel to Test the Surface- Piercing Propellers (SPP); Case Study Water Tunnel of Babol Noshirvani University of Technology*. International Journal of Maritime Technology, v.6 , p. 19- 30

[12]. Shora, M.M., Ghassemi, H., Nowruzi, H., (2017), *Using computational fluid dynamic and artificial neural networks to predict the performance and cavitation volume of a propeller under different geometrical and physical characteristics*. Journal of Marine Engineering & Technology, V.17 (2), p. 59- 84.

[13]. Yari, E., (2017), *Time Domain Analysis of the Ventilation around the Partial Immersed Propeller Using Sliding Mesh Method*. International Journal of Maritime Technology, V.7 , p. 19- 27.

[14]. Javanmardi, N., Ghadimi, P., Tavakoli, S., (2018), *Probing into the effects of cavitation on hydrodynamic characteristics of surface piercing propellers through numerical modeling of oblique water entry of a thin wedge*. Brodogradnja: Teorija i praksa brodogradnje i pomorske tehnike, V. 69 (2), p. 151- 168.

[15]. Seyyedi, S.M., Shafaghat, R., Gao, Z., (2018), *A Review on the Hydrodynamic Characteristics of the SPP Concerning to the Available Experimental Data and Evaluating Regression Polynomial Functions*. International Journal of Maritime Technology, V. 10 , p. 25- 35.

[16]. Yang, D., Ren, Z., Guo, Z., (2018), *Numerical Analysis on the Hydrodynamic Performance of an Artificially Ventilated Surface-Piercing Propeller*. Journal of Water, V. 10 (11), p. 2- 13.

[Downloaded from ijmt.ir on 2026-09-10]

[17]. Gangi Rad, R., Shafaghat, R., Yousefi, R., (2019), *Numerical investigation of the immersion ratio effects on ventilation phenomenon and also the performance of a surface piercing propeller*. Applied Ocean Research, V. 89, p. 251–260.
[18]. Nouroozi, H., Zeraatgar, H., (2019), *A reliable simulation for hydrodynamic performance prediction of surfacepiercing propellers using URANS method*. Applied Ocean Research, V. 92, 101939.
[19]. Seyyedi, S.M., Shafaghat, R., Siavoshian, M., (2019), *Experimental study of immersion ratio and shaft inclination angle in the performance of a surface-piercing propeller*. Journal of Mechanical Sciences, V. 10(1),p. 153-167.
[20]. Javanmard, E., Yari, E., Mehr, J.A., Mansoorzadeh, S., (2019), *Hydrodynamic characteristic curves and behavior of flow around a surface-piercing propeller using computational fluid dynamics based on FVM*. Applied Ocean Research V. 192, 106445.
[21]. Yari, E., Moghadam, A.B., (2020), *Inclination angle effect on ventilation pattern and trailing wake formation of the partially submerged propeller*. International Journal of Maritime Technology, V. 13 , p. 11- 19.
[22]. Yari, E., Moghadam, A.B., (2020), *BEM applied to the cup effect on the partially submerged propeller performance prediction and ventilation pattern*. Marine Engineering & Technology.
[23]. Seyyedi, S. M., Shafaghat, R., (2020), *A review on the Surface-Piercing Propeller: Challenges and opportunities*. Journal of Engineering for the Maritime Environment. V. 232, p. 1- 28.
[24]. Orca3D User Manual, 2016, Leveraging the power of Rhino for the naval architect, by DRS Technologies, Version 1.3.4.
[25]. STAR CCM+, Product Version of Simcenter STAR-CCM+ 2019.1 Build 14.02.010.
[26]. STAR CCM+, User guide, 2019.1 Build 14.02.010.
[27]. *Ship resistance and propulsion*, Practical Estimation of propulsive power, Univercity of southamptpon.

[Downloaded from ijmt.ir on 2026-09-10]